

Sara Rastgarnia^a, Khalil Ranjbar^a, Khalil A. Gheisari^a, Gholam H. Borhani^b

^aDepartment of Materials Science and Engineering, Faculty of Engineering, Shahid Chamran University of Ahvaz, Iran

^bDepartment of Materials Science, Malek-Ashtar University of Technology (MUT), Shahin-Shahr, Isfahan, Iran

Synthesis and characterization of mechanically alloyed cerium oxide reinforced Al-4.5 Mg alloy composite

Al-4.5 Mg-0.5 Mn alloy powders were mechanically alloyed by the addition of 1–3 wt.% cerium oxide (CeO_2) nanoparticles using a planetary ball mill under a dry argon atmosphere. A milling speed of 300 rpm and ball to powder ratio of 20:1 was used for all samples. An optimum milling time of 20 h was chosen considering the morphological and structural changes in the milled powders. The composite powders were consolidated via vacuum hot pressing at 515 °C. Mechanical properties were evaluated by hardness and compression tests. The evolution of the structure and microstructure during the milling process was studied the X-ray diffraction technique and field emission scanning electron microscopy, respectively. The corrosion behavior of the samples was investigated by potentiodynamic polarization testing in a standard 3.5 % chloride salt solution and assessed in terms of pitting potential and passivation range. CeO_2 reinforced mechanically alloyed Al–4.5 Mg exhibited a major improvement in its hardness and compressive strength compared to the un-reinforced base alloy, i.e. 40 and 50% increment respectively. Nevertheless, the most important effect of CeO_2 incorporation was observed in the pitting resistance of the alloy.

Keywords: Al-4.5 Mg alloy; Mechanical alloying; Cerium oxide; Pitting resistance

1. Introduction

Mechanical alloying (MA) is a solid-state powder processing technique involving the repeated welding, fracturing, and re-welding of powder particles in a high-energy ball mill [1]. This processing technique is also known as a powder metallurgy (P/M) route. P/M processing is usually preferred to conventional casting since a more homogeneous solid solution of alloying elements, as well as the uniform dispersion of the fine reinforcements in the matrix, is easier to achieve [1, 2]. This processing technique has now been widely accepted to synthesize a variety of MA products including oxide dispersion strengthened (ODS) metal matrix composites. In general, dispersion of nano-sized oxides particles into the aluminum matrix results in a significant improvement in matrix properties.

A lot of research has focused on the addition of low percentages of oxide particles to the Al matrix by mechanical

alloying [3–7]. Al–Mg nanocomposite reinforced by 5 wt.% Al_2O_3 particles fabricated by MA and its mechanical properties studied by Safari et al. [3]. They reported that after 10 h of high energy ball milling, a complete solid solution of Al–Mg was formed and the microhardness of the matrix increased dramatically due to the grain refinement and the solid solution formation. In another study, Tousei et al. [8] revealed that submicron α -alumina particles have a great influence on the size, morphology and pressability of the Al matrix composite powder produced by high energy ball milling. Their report showed that the distribution of the alumina particles in the Al matrix is homogeneous when the steady state is attained. A further study by Kang et al. [4] reported the hardness and tensile properties of nanometric Al_2O_3 particulate reinforced aluminum matrix composites prepared through the P/M technique. They found that hardness and tensile strength increased with the volume fraction of reinforcement, but strengthening leveled off above 4 vol.% Al_2O_3 due to clustering. The mechanically driven reduction reaction of metal oxides by aluminum has also been studied frequently. Arami et al. [6] studied the reactive reactions in an Al–CuO composite powder produced by high energy mechanical milling. Their report indicated that it is possible to synthesize nanocomposites with a more uniform distribution of the reinforcement particles using the internal oxidation method.

Nevertheless, the formation of a thermodynamically stable oxide film (Al_2O_3) on aluminum powder particles is a major problem during the pressureless sintering of these powders. This oxide film acts as a barrier to the inter-particle diffusion of aluminum atoms, retarding solid state sintering. Thus, it is necessary to chemically reduce, or mechanically disrupt the oxide layer to aid sintering. In the latter case, hot pressing is one of the sintering methods where the simultaneous application of uniaxial pressure and high temperature can accelerate the rate of densification.

Cerium oxide, as an ODS, is a promising option for improving the pitting resistance and mechanical strength of the aluminum matrix [9, 10]. On the other hand, Al5083 alloy is one of the major Al–Mg compositions, well-known for its high strength and desirable properties for structural applications. Furthermore, this alloy shows good weldability and formability. Therefore, the aim of this work was to simultaneously improve the mechanical properties and corrosion resistance of the Al-4.5Mg alloy by the fabrication of

CeO₂ reinforced Al-4.5Mg composites via the MA technique and hot press sintering. To our knowledge, so far no work has been done with the specific addition of cerium oxide as an ODS to Al5083 matrix via P/M route.

2. Experimental procedure

Al alloy powders composed of (Al, 4.5Mg, 0.5Mn) were ball milled along with 1–3 wt.% of CeO₂ nano particles of size ~40 nm in a Fritsch type planetary ball mill (Sepahan Tajhiz Iran) for 20 h. Four batches of samples were prepared and named C0, C1, C2, and C3, containing 0, 1, 2, and 3 wt.% CeO₂, respectively. The average particle size for Al, Mg and Mn was 56 μm, 98 μm and 10 μm, respectively. The vial of the ball-mill and the milling media were made up of stainless steel. The container was loaded with a blend of balls (∅ = 10 mm, mass = 5 g and ∅ = 20 mm, mass = 32.7 g). The total weight of the powder was about 10 g. The ball-to-powder mass ratio was selected at 20:1 and milled in an argon atmosphere with a milling speed of 300 rpm for 15 min on- and off-cycles, respectively. 2 wt.% of stearic acid (CH₃(CH₂)₁₆CO₂H) was added as a process control agent in order to prevent re-welding and promote the fracturing of powder particles.

Phase analysis of the milled powder was conducted before the addition of CeO₂ particles using an X-ray diffractometer (Philips) with a Cu-K_α radiation wavelength of 1.54056 nm. Structural parameters, including average crystallite size and lattice strain (microstrain), were evaluated based on X-ray diffraction (XRD) line broadening of the most intense diffraction lines of the Al alloy matrix (i.e., (111), (200), (220) and (311) planes). For this purpose, a single-line method was applied. In this method the mean lattice distortion, e , and average crystallite size, D , were calculated as follows [11]:

$$e = \frac{\beta_{\text{strain}}}{4 \tan \theta}, \quad D = \frac{\lambda}{\beta_{\text{size}} \cos \theta}$$

where λ is the wavelength of the X-ray source, θ is the diffraction angle and β_{strain} and β_{size} are the strain and lattice strain components of the integral breadth, respectively, calculated using the following equations:

$$\beta_{\text{strain}} = \sqrt{\beta_{\text{obs}}^2 - \beta_{\text{std}}^2}, \quad \beta_{\text{size}} = \beta_{\text{obs}} - \beta_{\text{std}}$$

where β_{obs} and β_{std} are the magnitude of observed and instrumental broadening, respectively. These structural parameters were estimated by means of a commercial software package [11].

Cerium oxide incorporated composite powders after milling were degassed at 380 °C under an argon atmosphere, and consolidated under an uniaxial load of 300 MPa. Subsequently, the samples were sintered in vacuum at 515 °C using a heating rate of 10 °K min⁻¹, held at this temperature for 30 min and then a uniaxial pressure of 100 MPa was applied for 30 min while maintaining the temperature. Hot pressing (HP) sintering was conducted in an HP furnace (Model MUT-HP 100T), and a cylindrical steel die with a sample size of 45 mm diameter and 15 mm height was used. The morphology of the ball milled powders and sintered pellets was studied in a field emission scanning electron microscopy (FESEM) (model: MIRA3

TESCAN) equipped with EDS (energy dispersive spectrometer). Microhardness measurements were performed using a Vickers hardness tester with a load of 200 g for an indentation time of 10 s. The density of the hot pressed samples was measured based on conventional Archimedes' principle conventions. Compression testing was performed on the hot pressed samples according to ASTM-E9 standard [12] at a constant displacement rate of 1 mm s⁻¹. Sub-sized cylindrical samples were machined from the middle of hot pressed pellets with a L/D of 1.5 (with the length and diameter of 9 and 6 mm respectively).

To conduct the potentiodynamic polarization tests, the samples were cut from the center of the hot pressed samples and prepared according to the ASTM-G3 standard [13]. All corrosion tests were conducted in a 3.5% NaCl solution prepared by dissolving 35 g of NaCl in double distilled water, at a scan rate of 0.5 mV s⁻¹ using an AUTO LAB potentiostat–galvanostat (model: AUT8491). The temperature and the pH of the electrolyte were maintained at 25 °C and 7, respectively. An electrochemical cell consisting of platinum as the auxiliary electrode, saturated calomel as the reference electrode, and the hot pressed samples as the working electrode was used. Before each polarization, the sample was immersed in the test solution for 30 min at the open circuit potential (OCP), allowing the system to stabilize. An exposure area of 25 mm² was subjected to the corrosion tests and the rest of the areas were covered with epoxy. The i -corrosion was calculated using Tafel extrapolation [14].

3. Results and discussion

3.1. Mechanical milling

The initially selected powders were mixed and milled for different milling times; from 5–20 h. Figure 1 shows the effect of milling time on the morphology of the milled powders. After 5 and 10 h of milling (Fig. 1a and b), the particles were severely deformed and flattened and had a flake-like morphology. The state of cold welding is also visible in this image. As depicted in Fig. 1c, the particles attained an almost equiaxed morphology after 20 h of milling. Apparently, at this stage of milling, the particles became more rounded in shape and finer in average size. This suggested that the predominant processes at this stage were cold working and fracturing. The morphology of the as-received CeO₂ nano particles is shown in Fig. 1d.

The evolution of crystallite size, lattice strain and solid solution formation at different milling times were examined by XRD. Figure 2a shows the XRD patterns of the milled powders. It reveals that after 5 and 10 h of milling, the characteristic diffraction lines corresponding to Al and Mg were noticed in the patterns. But, after 20 h of milling, Mg peaks disappeared completely, which indicates the formation of the fcc supersaturated solid solution of Al–Mg (Al(Mg)_{ss}). It seems that 20 h of high energy milling created sufficient particle size reduction, defect density accumulation, and a local rise in temperature to aid the diffusion of Mg into the Al lattice. There was also a clear shift in Al peaks towards lower angles (Fig. 2b), due to the solution of the larger Mg atoms into the Al matrix, which further proves completed solid solution formation. The results correspond with earlier studies [3, 15–17]. A similar trend of solid solution for-

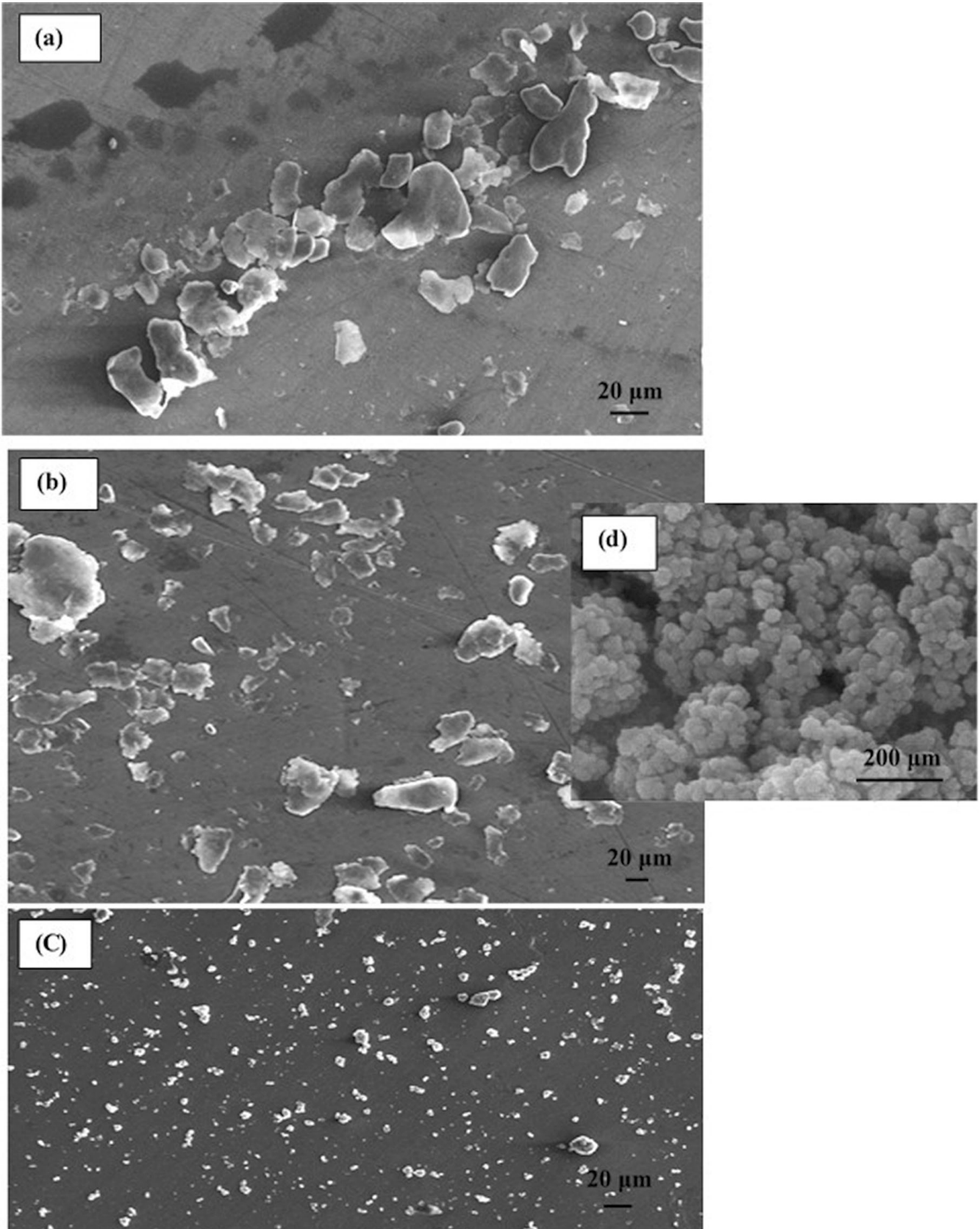


Fig. 1. Change in morphology of Al-4.5Mg powders milled for: (a) 5 h, (b) 10 h, and (c) 20 h. SEM micrographs reveal that particles are flake-like after 5 and 10 h milling, and alter their morphologies to more spherical shape and smaller size with further milling. (d) SEM micrograph of as-received cerium oxide nano-particles.

mation was also observed for cerium oxide incorporated samples. The XRD pattern of C3 sample is presented in Fig. 3.

Variations of $\text{Al}(\text{Mg})_{\text{ss}}$ crystallite size and lattice strain as functions of milling time are presented in Fig. 4a. The application of high energy milling induces the repeated welding–fracturing of particles, severe plastic deformation, work hardening, and various types of lattice defects (vacancies, grain boundaries, dislocations) in the matrix [2]. The consequences of these phenomena are the crystallite refinement and lattice strain increment. These trends have also been observed by Azimi et al. [15], Safari et al. [3] and Yazdian et al. [18] for different mechanically alloyed Al–Mg alloys. In the present study, supersaturated $\text{Al}(\text{Mg})_{\text{ss}}$ solid solution exhibited a crystallite size and lattice strain of about 17 nm and 0.63 %, after 20 h of milling respectively. The change in the $\text{Al}(\text{Mg})_{\text{ss}}$ lattice parameter as a function of milling time is presented in Fig. 4b. As can be seen, the $\text{Al}(\text{Mg})_{\text{ss}}$ lattice parameter increases due to the dissolution of bigger size Mg atoms into the Al, forming a supersaturated Al–Mg solid solution. The $\text{Al}(\text{Mg})_{\text{ss}}$ lattice parameter was determined using the highest-angle peak ((311) planes) for the sake of greater accuracy according to the method given in Ref. [19].

3.2. Densification

In order to overcome the pressureless sintering of Al composites due to the formation of an aluminum oxide layer

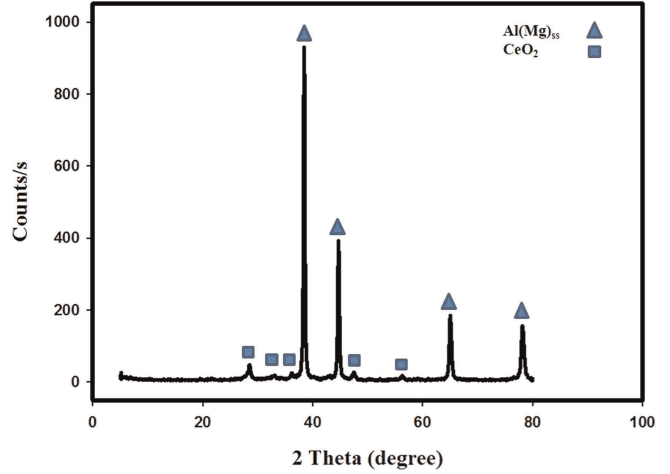


Fig. 3. X-ray diffraction patterns of Al-4.5Mg/CeO₂ powder mixtures (C3 sample) milled for 20 h.

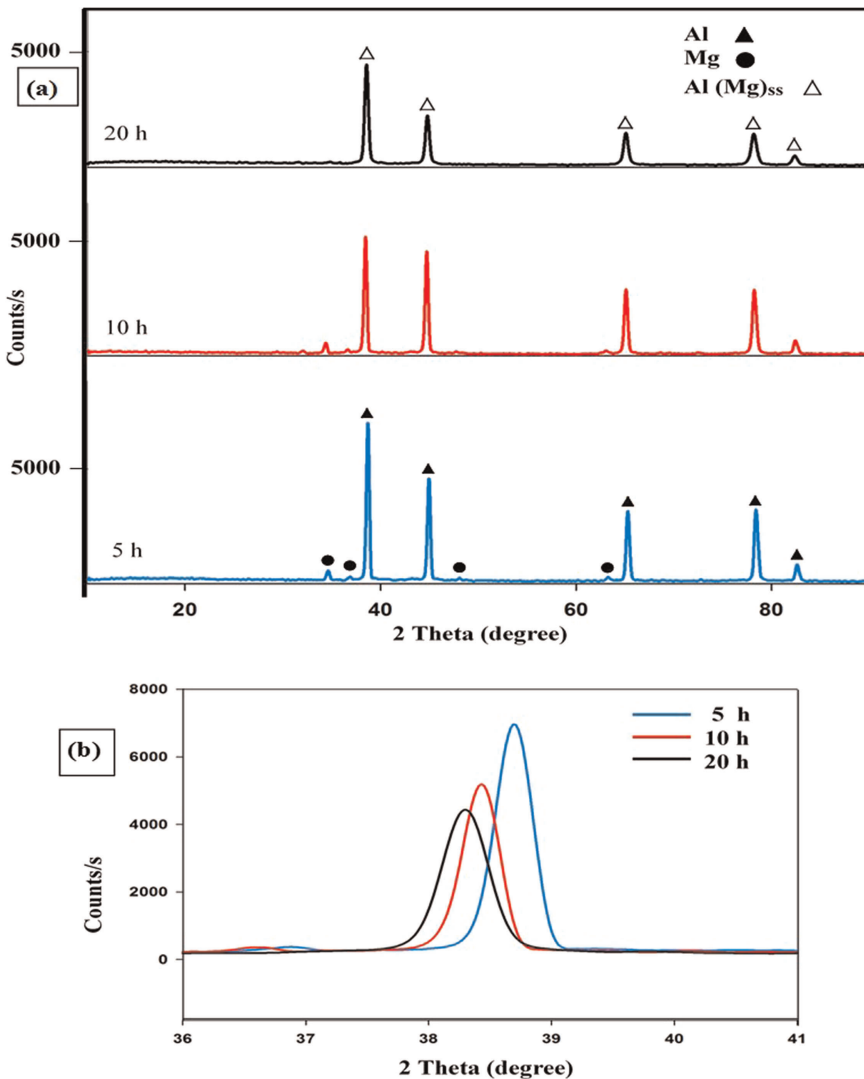


Fig. 2. X-ray diffraction patterns of Al-4.5Mg/CeO₂ powder mixtures (a) milled for different lengths of time, and (b) shifting of Al (111) peak during milling.

which acts as a barrier for the diffusion, sintering was done by the hot pressing technique under argon atmosphere. In this process, elevated temperature and compressive stress were applied simultaneously to consolidate the green compacted powders into sintered components. Pressure disrupts the oxide layer and increases the driving force for densification; in effect, reducing the sintering temperature. Hot pressing also results in smaller grain size compared to conventional sintering. The density of the samples after hot pressing was measured, and the corresponding results are reported in Table 1. It shows that sintering density slightly decreases with increasing CeO₂ content. Actually, the sintering density of the base alloy with no CeO₂ content, was 97% and it dropped to 95% with the addition of 3 wt.% CeO₂. Akbarpour et al. [20] reported a similar result using SiC reinforcement in a Cu matrix fabricated with HP. The reduction in sintered density with an increasing amount of reinforcement could be attributed to the thermally stable CeO₂ particles, which impeded bonding within the matrix powder particles and increased the diffusion distance during the sintering stage.

Figures 5 and 6 present the mechanically alloyed bulk material microstructures after HP. In the case of base alloy (C0 sample), micrograph (Fig. 5a) revealed a large number of gray color Al-Fe-Mn intermetallic compounds on the polished surface. A more uniform distribution of white color CeO₂ particles was observed in the case of sample C1 (Fig. 5b) on its cross-sectional area parallel to the pressing direction. In this case, a least amount of oxide particles was added. The distribution of CeO₂ particles was also fairly uniform with 2 wt.% shown in Fig. 6a, but further addition of CeO₂ beyond 2 wt.% resulted in agglomeration and particle free zones, as shown in Fig. 6b. This in turn, affected the sintered density, as reported in Table 1. The

Table 1. variation of sintered density as function of cerium oxide additions.

Sample	C0	C1	C2	C3
Relative sintered density (%)	97	97	96	95

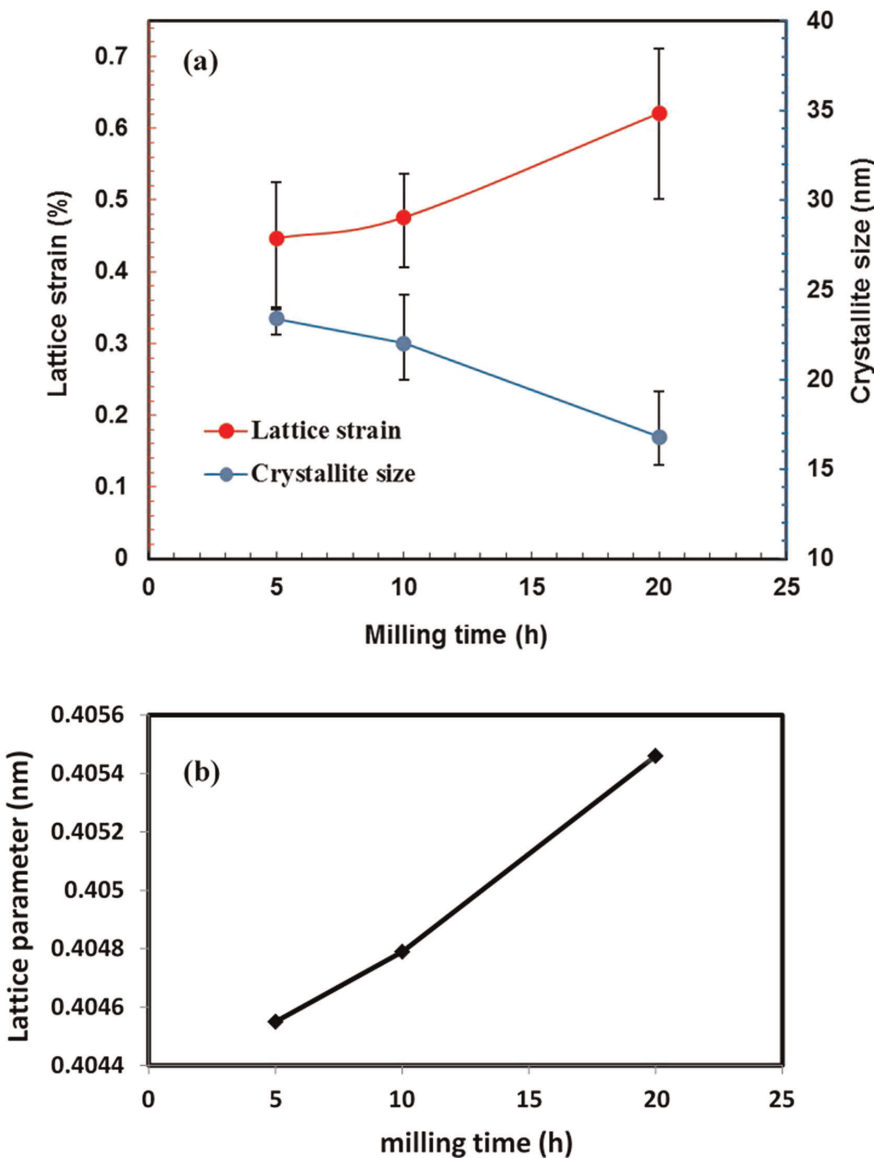


Fig. 4. (a) Evolution of crystallite size and lattice strain as a function of milling time, and (b) change in lattice parameter of base metal as a function of milling time.

white and the gray color particles mentioned earlier were identified to be CeO_2 and $\text{Al}_6(\text{Fe-Mn})$ intermetallic compounds, respectively. Their respective EDS spectra are shown in Figs. 7a and b respectively. As can be seen, a significant Al signal is observed in the EDS microanalysis spectrum of the cerium oxide particles. Since the minimum resolution limit of the microchemical analysis using SEM-EDS analysis is about $1\ \mu\text{m}$ [21], and on the other hand, the mean CeO_2 particle size in the studied microstructure is less than $0.5\ \mu\text{m}$, the microchemical results include surrounding Al-base matrix; therefore, a significant signal of Al is observed in Fig. 7a. Furthermore, iron as a major impurity, was introduced into the powder during the milling operation.

3.3. Mechanical properties

Hardness and compression tests were conducted to assess the mechanical properties of the HPed samples. Figures 8 and 9 depict the results, respectively. The average hardness

values of CeO_2 reinforced composites were considerably higher than those obtained for the base alloy (C0 sample). The average hardness value of the C3 sample is 180 VHN compared to 128 VHN for the C0 sample with no reinforcement, i. e., $\sim 40\%$ increment. The increase in hardness with the addition of CeO_2 content is attributed to grain/crystallite size reduction (Fig. 4a), and due to the harder nature of CeO_2 nano particles, which cause locally high internal strain in the Al matrix because of their hardness and resistance to deformation, and have a work-hardening effect on the matrix. Safari et al. [22] have also reported a similar hardness increment in the mechanically alloyed Al-Mg matrix reinforced by Al_2O_3 particles.

The stress-strain curves for the HPed samples with different weight percentages of CeO_2 nanoparticles are shown in Fig. 9. The fabricated composites exhibit enhanced com-

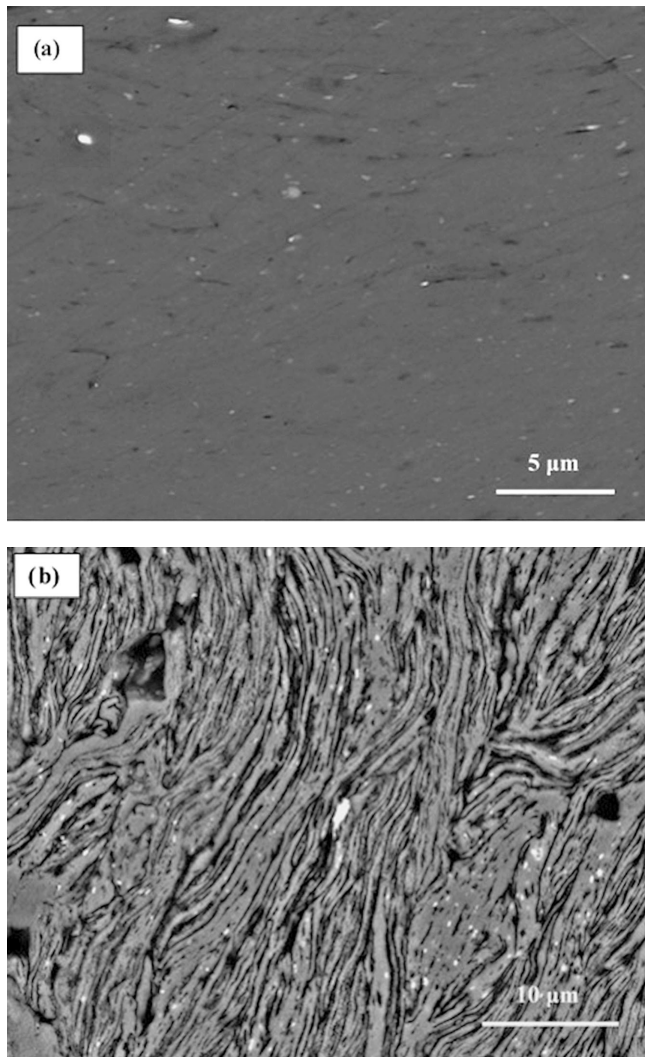


Fig. 5. (a) Scanning electron micrograph shows the matrix of Al-4.5Mg alloy (C0 sample) after hot pressing, with no reinforcing particles but with a lot of primary intermetallic particles (gray in color) distributed throughout the matrix, and (b) cross-section of C1 sample parallel to pressing direction. It shows that fine CeO_2 reinforcing particles (white in color) have homogeneously distributed with in the matrix.

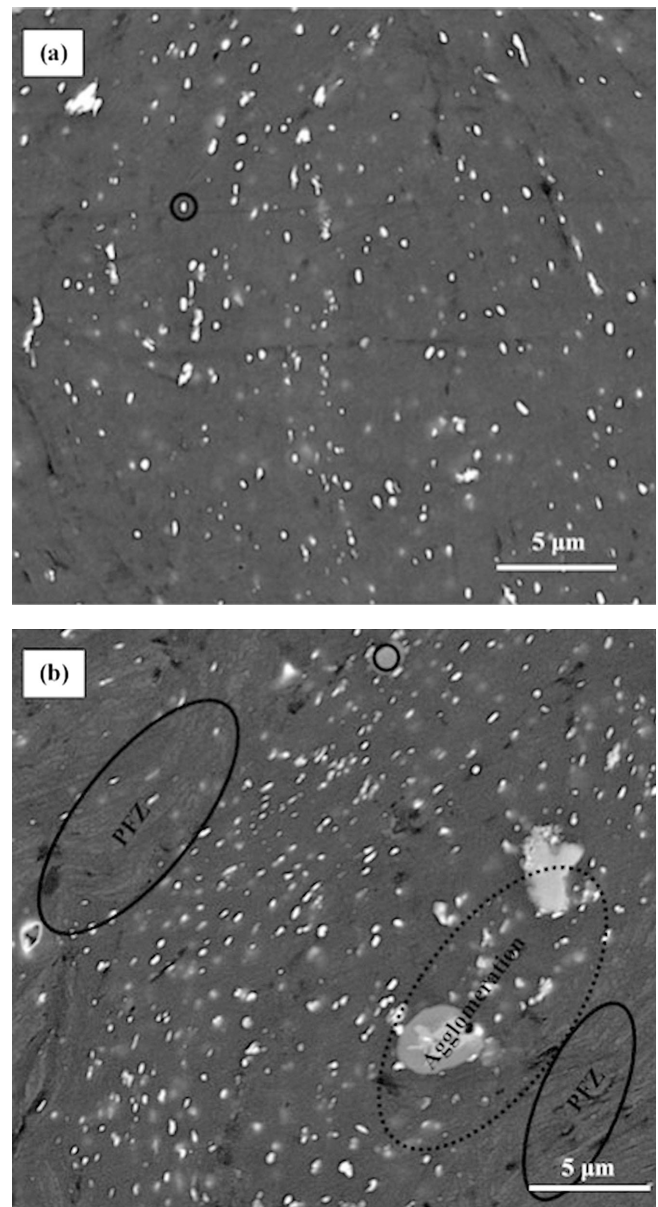


Fig. 6. Distribution of CeO_2 reinforcing particles after hot pressing with in the matrix of Al-4.5 Mg alloy: (a) C2 sample, and (b) C3 sample. In the latter case, with increasing CeO_2 content, particle free zone (PFZ) and agglomeration of the reinforcing particles are noticed.

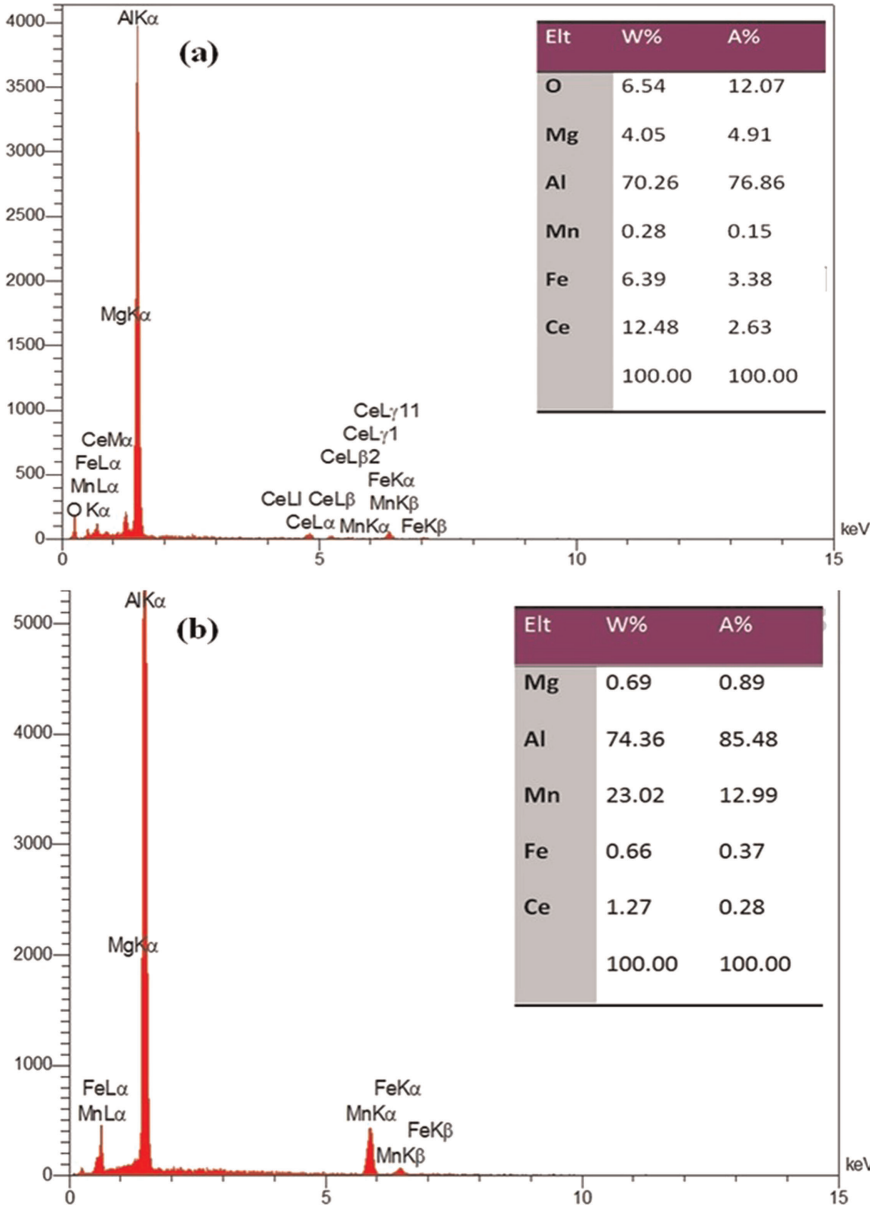


Fig. 7. (a) SEM-EDS analysis of cerium oxide particles that are bright and are shown by a solid circle in Fig. 6a, and (b) SEM-EDS analysis corresponding to $Al_6(Mn,Fe)$ intermetallic compound which is fragmented and redistributed after milling and hot pressing. These gray particles are marked by a solid circle in Fig. 6b.

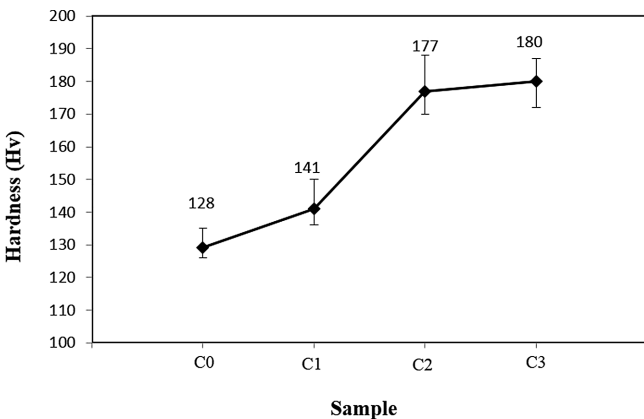


Fig. 8. Variation of Vickers hardness as a function of cerium oxide content after hot pressing.

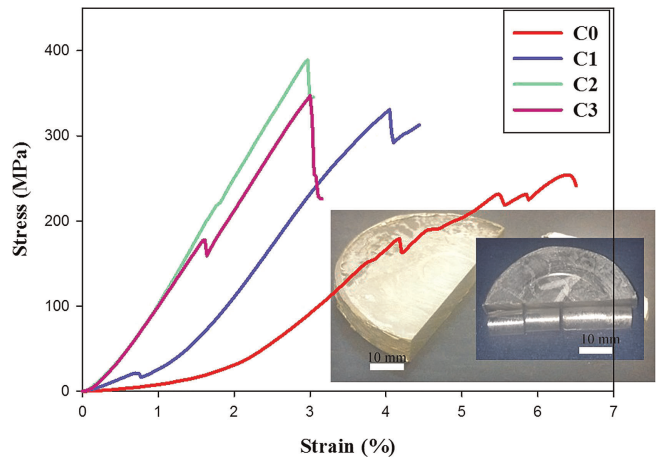


Fig. 9. Compression stress-strain curves of different hot pressed samples. The macrograph at the center shows the hot pressed sample that is cut and machined to prepare the cylindrical compression test specimens.

pressive strength compared to that of the base alloy (C0) sample. The maximum compressive strength of 350 MPa is obtained for the C2 composite, i.e., an enhancement of $\sim 50\%$, compared to the unreinforced C0 sample with a compressive strength of 280 MPa. The addition of CeO_2 particles beyond 2 wt.% leads to the agglomeration and reduction of sintered density; hence, a drop in compressive strength is observed in the C3 sample. The increase in the compressive strength of Al–Mg/ CeO_2 composites is ascribed to various mechanisms; a) Strengthening by the Orowan mechanism [23–24] since CeO_2 particles are nano-sized and homogeneously dispersed throughout the matrix, b) grain size strengthening due to the repeated welding and fracturing of particles by high energy milling, which also leads to solid solution formation, c) the enhanced dislocation density due to the residual plastic strain caused by the difference in the coefficients of thermal expansion between the Al–Mg solid solution (matrix) and the reinforcing CeO_2 particles, and d) the fragmentation and uniform distribution of primary intermetallic compounds which act as reinforcement. These mechanisms are reported in some relevant studies, [3, 20], [23], [25], and [10], respectively. The relative contribution of the strengthening effects by the listed mechanisms needs further investigation.

3.4. Corrosion behavior

The corrosion behavior of the HPed samples was studied by performing potentiodynamic polarization tests [13]. The results are presented as potentiodynamic polarization curves in Fig. 10. The corrosion potential (E_{corr}), pitting potential (E_{pit}) as well as the corrosion current density (i_{corr}) derived from these curves are summarized in Table 2. In general, the corrosion of aluminum and its alloys initiates from the oxide film formation on its surface when it is exposed to air or water. In other words, an intersection anodic curve with a cathodic curve appeared in the passive region of the alloy causing a low corrosion rate attributed to the protective passive film formed on the surface. This oxide film may dissolve and result in localized corrosion (pits) when it is exposed to alkaline solutions. Pits can initiate at locations such as phase boundaries, insoluble intermetallic compounds, interface regions between matrices and reinforcements, as a result of the difference in corrosion potential within a localized galvanic cell at the alloy surface. A

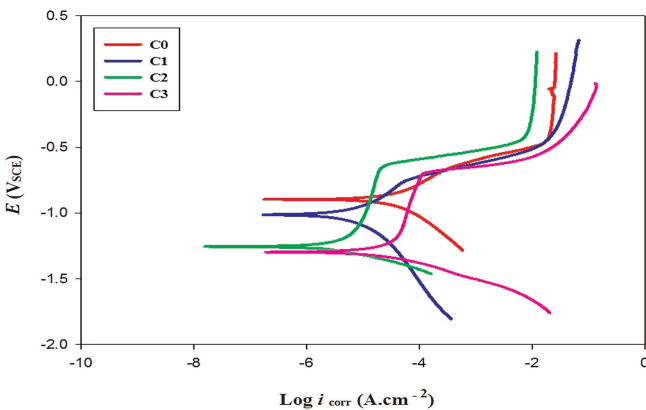


Fig. 10. Potentiodynamic polarization curves of the HPed samples in 3.5% NaCl solution.

critical potential called (E_{pit}) is defined in order to quantify the resistance of material to pitting corrosion. At this potential, the localized breakdown of the oxide film is initiated. Similarly, a repassivation or protection potential is defined which represents the minimum potential at which existing pits can propagate, but new pits cannot form. In general, material with higher (E_{pit}) is more resistant to pitting corrosion. Likewise, the difference between (E_{pit}) and (E_{corr}) in a given environment is considered as a measure of the susceptibility to localized corrosion [26]. Considering this concept, in this study, a comparison was made between the corrosion response of the Al–Mg base alloy and CeO_2 incorporated composites. It was found that composite samples had a relatively lower i_{corr} and a significantly higher passivation range than the base alloy; therefore, a relatively better corrosion response was obtained due to the effect of the CeO_2 particles. The best corrosion response was obtained for the 2 wt.% cerium oxide incorporated composite (i.e., the lowest i_{corr} and the longest passive region $E_{\text{pit}} - E_{\text{corr}}$).

The improved pitting resistance was definitely attributable to the effect of cerium oxide, which is considered as an effective cathodic inhibitor in aluminum matrix. Ashraf et al. [9] reported a similar positive effect of cerium oxide on the corrosion behavior of an aluminum matrix, when they melted aluminum ingot and added cerium oxide to the melt by stirring. Hossieni et al. [10] also observed the same effect in cerium oxide incorporated Al5083 surface composites fabricated by friction stir processing. It is believed that the cerium oxide in an aluminum matrix can suppress corrosion reactions by creating barriers to the supply of oxygen and electrons from the aluminum matrix to the corrosion medium [27].

4. Conclusion

Cerium oxide reinforced Al-4.5 Mg alloy composites were fabricated by mechanical alloying and hot pressing. The microstructural features, mechanical properties, and corrosion behavior of these composites were evaluated. Based on the results obtained, the following conclusions can be drawn:

1. By increasing milling time, crystallite sizes reduced (to ~ 17 nm) and lattice strain increased (to 0.63%). A complete solid solution of Mg in Al matrix was obtained after 20 h of milling. This was inferred from the clear shift of the Al peaks toward lower angles and a slight lattice expansion due to the substitution of larger Mg atoms in the Al lattice and grain refinement.

Table 2. Summary of potentiodynamic polarization test results conducted in a 3.5% NaCl solution at room temperature for different HPed samples.

Sample	i_{corr} ($\mu\text{A cm}^{-2}$)	E_{corr} (mV)	ΔE (mV) ($E_{\text{pit}} - E_{\text{corr}}$)
C0	28.18	-894	–
C1	4.786	-1012	163
C2	1.584	-1263	553
C3	14.12	-1297	545

2. Sintered density dropped slightly with the addition of cerium oxide particles. Relative density dropped to 95 % with 3 wt.% oxide particles from its initial value of 97 % with no oxide particles. This is because CeO₂ ceramic particles are thermally stable, have no solubility in aluminum matrix, and impede bonding between the matrix powder particles. As a result, they increase the diffusion distance during the sintering stage, resulting in a decrease in the relative density.
3. The hardness values of the reinforced composites were increased with the addition of CeO₂ particles compared to that of the un-reinforced base alloy (a ~40 % increment with 3 wt.% CeO₂). Nonetheless, maximum compressive strength (~50 % increment) was attained with 2 wt.% CeO₂, above which strengthening declined due to agglomeration. The uniform distribution of non-sized CeO₂ particles acted as reinforcement and resulted in a work-hardening effect on the matrix, leading to enhancement of mechanical properties. Additionally, grains were refined and the intermetallic particles were fragmented and distributed well throughout the matrix after mechanical alloying.
4. The incorporation of nano-sized cerium oxide particles into the Al-4.5Mg base alloy resulted in a remarkable increase in the pitting resistance of the alloy, by acting as effective cathodic inhibitors.

The authors highly appreciate the financial support provided by Shahid Chamran University of Ahvaz, Iran.

References

- [1] C. Suryanarayana: *Prog. Mater. Sci.* 46 (2001) 1. DOI:10.1016/S0079-6425(99)00010-9
- [2] C. Suryanarayana, N. Al-Aqeeli: *Prog. Mater. Sci.* 58 (2013) 383. DOI:10.1016/j.pmatsci.2012.10.001
- [3] J. Safari, G.H. Akbari, A. Shahbazkhan, M. Delshad Chermahini: *J. Alloys Compd.* 509 (2011) 9419. DOI:10.1016/j.jallcom.2011.07.061
- [4] Y.C. Kang, S.L.I. Chan: *Mater. Chem. Phys.* 85 (2004), 438. DOI:10.1016/j.matchemphys.2004.02.002
- [5] S.M. Zebarjad, S.A. Sajjadi: *Mater. Design* 28 (2007) 2113. DOI:10.1016/j.matdes.2006.05.020
- [6] H. Arami, A. Simchi: *Mater. Sci. Eng.: A* 464 (2007) 225. DOI:10.1016/j.msea.2007.01.143
- [7] S. Kleiner, F. Bertocco, F.A. Khalid, O. Beffort: *Mater. Chem. Phys.* 89 (2005) 362. DOI:10.1016/j.matchemphys.2004.09.014
- [8] S.S. Razavi Tousi, R. Yazdani Rad, E. Salahi, I. Mobasherpour, M. Razavi: *Powder Tech.* 192 (2009) 346. DOI:10.1016/j.powtec.2009.01.016
- [9] P.M. Ashraf, S. Shibli: *Electrochem. Com.* 9 (2007) 443. DOI:10.1016/j.elecom.2006.09.010
- [10] S.A. Hosseini, K. Ranjbar, R. Dehmolaie, A.R. Amirani: *J. Alloys Compd.* 622 (2015) 725. DOI:10.1016/j.jallcom.2014.10.158
- [11] Th.H. de Keijser, J.I. Langford, E.J. Mittemeijer and A.B.P. Vogels: *J. Applied Cry.* 15 (1982) 308. DOI:10.1107/S0021889882012035
- [12] American Society for Testing Materials: Standard test method of compression testing of metallic materials at room temperature. ASTM E9-09. ASTM International, West Conshohocken, Pennsylvania (2014).
- [13] American Society for Testing Materials: Standard practice for conventions applicable to electrochemical measurements in corrosion testing. ASTM G3-14, ASTM International, West Conshohocken, Pennsylvania (2014).
- [14] W.S. Tait: *An Introduction to Electrochemical Corrosion Testing for Practicing Engineers & Scientists*, Pair O Docs Pubns, Racine Wisconsin (1994).
- [15] A. Azimi, A. Shokuhfar, A. Zolriasatein: *Mater. Sci. Eng.: A* 595 (2014) 124. DOI:10.1016/j.msea.2013.11.094
- [16] M. Brochu, T. Zimmerly, L. Ajdelsztajn, E.J. Lavernia, G. Kim: *Mater. Sci. Eng.: A* 466 (2007) 84. DOI:10.1016/j.msea.2007.02.028
- [17] S. Scudino, M. Sakaliyska, K.B. Surreddi, J. Eckert: 14th International Symposium on Metastable and Nano-Materials (ISMANAM-2007) 483 (2009) 2. DOI:10.1016/j.jallcom.2008.07.161
- [18] N. Yazdian, F. Karimzadeh, M. Tavosi: *J. Alloys Compd.* 493 (2010) 137. DOI:10.1016/j.jallcom.2009.12.144
- [19] Cullity, B.D.: *Elements of X-ray diffraction*, 2nd edn. Addison-Wesley series in metallurgy and materials. Addison-Wesley, Reading, Mass., London (1978).
- [20] M.R. Akbarpour, E. Salahi, F. Alikhani Hesari, H.S. Kim, A. Simchi: *Mater. & Design* 52 (2013) 881. DOI:10.1016/j.matdes.2013.05.072
- [21] P.J. Goodhew, J. Humphreys, R. Beanland: *Electron Microscopy and Analysis*. Taylor & Francis, London (2001), pp. 189–194.
- [22] J. Safari, M. Delshad Chermahini, G.H. Akbari: *Powder Tech.* 234 (2013) 7. DOI:10.1016/j.powtec.2012.09.033
- [23] Z. Zhang, D.L. Chen: 14th Inter. Conf. Strength Mater. 483–484 (2008) 148. DOI:10.1016/j.msea.2006.10.184
- [24] R. George, K.T. Chen: *Scripta Mater.* 53 (2005) 1159. DOI:10.1016/j.scriptamat.2005.07.022
- [25] M.R. Akbarpour, E. Salahi, F. Alikhani Hesari, A. Simchi, H.S. Kim: *Mater. Sci. Eng.: A* 572 (2013) 83. DOI:10.1016/j.msea.2013.02.039
- [26] Cramer, S.D.: *ASM Handbook, Volume 13A: Corrosion: Fundamentals, Testing, and Protection*. Vol. 13 (2003).
- [27] Y. Xingwen, C. Chunan, Y. Zhiming, Z. Derui, Y. Zhongda: *Corr. Sci.* 43 (2001) 1283. DOI:10.1016/S0010-938X(00)00141-4

(Received December 30, 2016; accepted August 8, 2017)

Correspondence address

Khalil Ranjbar
Department of Materials Science and Engineering
Faculty of Engineering
Shahid Chamran University of Ahvaz
Iran
Tel.: +98 6133330020 19x5682
Fax: +98 6133336642
E-mail: k_ranjbar@scu.ac.ir

Bibliography

DOI 10.3139/146.111565
Int. J. Mater. Res. (formerly Z. Metallkd.)
108 (2017) E; page 1–9
© Carl Hanser Verlag GmbH & Co. KG
ISSN 1862-5282